

Post-critical *SsPmp* and Its Applications to Virtual Deep Seismic Sounding (VDSS)

1. Sensitivity to Lithospheric 1D and 2D Structure

Tianze Liu¹ (tianze@stanford.edu), Simon L. Klemperer¹, Chunquan Yu², Jieyuan Ning³

1. Department of Geophysics, Stanford University

2. Seismological Laboratory, California Institute of Technology

3. Institute of Theoretical and Applied Geophysics, School of
Earth and Space Science, Peking University

Key words: Seismology, body waves, teleseismic imaging, crustal imaging, crustal structure, lithospheric imaging, lithospheric structure, Virtual Deep Seismic Sounding

Abstract

Virtual Deep Seismic Sounding (VDSS) has recently emerged as a novel method to image the Moho and potentially other lithospheric boundaries. The behavior of *SsPmp*, the post-critical reflection phase at the Moho that is utilized in VDSS, is rich with complexities not yet widely utilized. Here, motivated by observations from the Ordos Plateau in North China, we use synthetic seismograms computed with a broad range of 1D models to evaluate how different parts of the lithosphere along the ray path of *SsPmp* affect its phase, amplitude, and arrival time. Our findings include: (1) When the crust-mantle boundary is a sharp discontinuity, the *SsPmp* phase shift relative to the direct S wave is controlled by lower-crustal V_p , upper-mantle V_p and ray parameter. This property indicates the possibility of using *SsPmp* to constrain V_p in the lower crust and uppermost mantle. (2) When the crust-mantle boundary is a velocity-gradient zone, *SsPmp* arrival times vary as different functions of ray parameter from cases with a sharp crust-mantle boundary, because different rays turn at different depths. This feature allows measurement of the vertical velocity gradient in the crust-mantle transition zone with *SsPmp*. (3) When the virtual source (location of S-to-P conversion at the free surface) is in a sedimentary basin, *SsPmp* amplitude can be significantly reduced due to low S-to-P reflected energy at the virtual source. This may cause the absence of *SsPmp* despite appropriate source-receiver geometry. In addition to 1D models, we further conduct 2D waveform modeling and find that the *SsPmp* arrival time relative to direct S is not only controlled by crustal thickness at the reflection point, but also by lateral variation of V_s beneath the virtual source and receiver. Therefore, in areas with significant lateral heterogeneity in the lithosphere the accuracy of crustal-thickness

measurements from *SsPmp* arrival times depends on our knowledge of the variability of lithospheric structure across a broad region.

1. Introduction

For a quarter-century the seismic community has relied heavily on receiver function (RF) techniques, which use teleseismic P-to-S (*Pms* or PRF) or S-to-P (*Smp* or SRF) converted phases, to image discontinuities in the lithosphere (Fig. 1) (e.g. Kind et al., 1995; Langston, 1979; Owens and Taylor, 1984). In recent years, Virtual Deep Seismic Sounding (VDSS) has emerged as a novel method to image the crust-mantle boundary (CMB) and has been successfully applied to multiple datasets from different areas to yield Moho depths independent from RF results (e.g. Kang et al., 2016; Liu et al., 2015; Parker et al., 2016; Tseng et al., 2009; Yu et al., 2012; Yu et al., 2016). Here we use *CMB* to denote the geological transition from crust to mantle, whether abrupt or a “velocity-gradient zone” spanning many kilometers; and *Moho* to denote a seismological inference about this transition, typically given as a single depth. Post-critical *SsPmp*, the seismic phase used in VDSS, originates when upcoming teleseismic S waves convert to down-going P waves at the free surface (the virtual source), and then undergo post-critical reflection at or within the CMB and finally reach the receiver (Fig. 1). Hereafter we use *SsPmp* to refer to post-critical *SsPmp* for simplicity. The arrival time of *SsPmp* relative to the direct S arrival (or *Ss*), hereafter T_{VDSS} , is used to estimate the Moho depth at the reflection point, normally assumed to be the midpoint between the virtual source and the receiver. Because VDSS uses teleseismic events, the incident S wave can be approximated as a plane wave with constant ray parameter. To enable post-critical reflection of *SsPmp* at the Moho, appropriate epicentral distances are $\sim 30\text{--}50^\circ$ (Yu et al., 2016), corresponding to ray parameter $p = \sim 0.1256\text{--}0.1409$ s/km for a focal depth of 0 km ($1/p = \sim 7.10\text{--}7.96$ km/s) (Kennett, 1991), and slightly smaller p for larger focal depths (Fig. 2). Due to post-critical reflection at the Moho, *SsPmp* usually has amplitude comparable to *Ss* (Fig. 3b), making it possible to construct a seismic profile with a single event recorded by an array (Figs. 4b,c). Because *SsPmp* undergoes post-critical reflection at the Moho, its phase is changed relative to *Ss* (Aki and Richards, 1980a)(Fig. 3b; hereafter referred to as phase shift for simplicity and denoted Φ_{VDSS}), making it difficult to directly pick T_{VDSS} from raw records. In order to establish a robust measure of *SsPmp* amplitude, we first separate vertical and radial component seismograms into pseudo-P (motion associated with

incoming P waves) and pseudo-S (motion associated with incoming S waves) components (hereafter P and S for simplicity) with a particle-motion analysis algorithm (Yu et al., 2013) so that Ss and $SsPmp$ appear only on S and P components respectively (Fig. 3b). We then compute the envelope functions of Ss and $SsPmp$ and define the ratio between the peak values of $SsPmp$ and Ss envelope functions as A_{VDSS} (Fig. 3b). Because envelope function is independent of phase shift, A_{VDSS} is a robust measure of $SsPmp$. For the simple single-layer-crust model in Fig. 3a, $A_{VDSS} = 0.86$. A_{VDSS} is not equal to one due to energy lost (1) at the virtual source when incident S waves generate reflected S waves and (2) at the Moho when down-going P waves generate reflected and transmitted S waves. For simplicity, in most of the following analyses when variation in $SsPmp$ amplitude is qualitatively shown, we normalize $SsPmp$ with the peak of Ss waveforms and use it as a proxy for A_{VDSS} . However, we note that whenever quantitative analysis of $SsPmp$ amplitude is required, A_{VDSS} should be calculated (discussed further in Section 3.3.2 below).

Most previous studies (e.g. Tian et al., 2015; Tseng et al., 2009; Yu et al., 2016;) used 1D waveform fitting to measure T_{VDSS} , and then found the trade-off relation between crustal V_p and thickness H using the equation:

$$T_{VDSS} = 2H \sqrt{\frac{1}{V_p^2} - p^2} \quad (1)$$

where p is the ray parameter of the incident S wave. In the process of waveform fitting, the upper mantle is commonly assumed to be a half space with V_p fixed *a priori* (e.g. Tian et al., 2015; Yu et al., 2016). Recently, Parker et al. (2016) proposed picking T_{VDSS} directly from the envelope function of $SsPmp$, because the envelope function is independent of the phase shift. For the purposes of waveform fitting, previous VDSS studies have commonly assumed that the CMB is a discontinuity in V_p , since Tseng et al. (2009) and Yu et al. (2012) have shown that $SsPmp$ waveforms appear similar whether the CMB is a velocity gradient zone or a discontinuity. Multiples (reverberations) generated in sedimentary basins severely contaminate receiver-function waveforms and have presented a long-standing challenge to the utility of receiver functions (e.g. Bao and Niu, 2017; Guan and Niu, 2017; Langston, 2011; Tao et al., 2014; Yu et al., 2015). In contrast, the manner in which sedimentary basins affect $SsPmp$ waveforms is not widely understood. Parker et al. (2016) showed that $SsPmp$ varies with velocity variation within basins, and Ferragut et al. (2017) searched for but did not find effects from a <1-km thick basin.

Here we present as motivation a dataset from the Ordos Plateau in North China in which significant changes in *SsPmp* phase shift, amplitude, and travel time (Φ_{VDSS} , A_{VDSS} , T_{VDSS}) are observed across the recording array. We first use synthetic waveforms to demonstrate that, when the CMB is a sharp discontinuity, Φ_{VDSS} decreases from $\sim 180^\circ$ to $\sim 0^\circ$ as the lower crustal V_p (hereafter V_p^{lc}) or upper mantle V_p (hereafter V_p^{um}) or ray parameter p increases. Additionally, when p is small ($1/p$ is close to V_p^{um}) Φ_{VDSS} is more sensitive to V_p^{um} than V_p^{lc} , whereas when p is large ($1/p$ is close to V_p^{lc}) Φ_{VDSS} is more sensitive to V_p^{lc} than V_p^{um} . We next show that when the CMB is a velocity gradient zone with thickness up to the dominant wavelength of incident S wave (S_s), neither Φ_{VDSS} nor A_{VDSS} varies significantly with p , but T_{VDSS} varies as different functions of p from the case with a sharp CMB, because rays with different ray parameters turn at different depths within the velocity-gradient zone. This feature should make VDSS an ideal method to study CMB structure in areas such as the Colorado Plateau, where a sharp Moho is not observed by traditional methods based on pre-critical reflections and conversions (Hauser and Lundy, 1989; Shen et al., 2013). We also demonstrate that although A_{VDSS} is largely insensitive to CMB structure, it is significantly decreased by low near-surface velocity at the virtual source, which may explain cases of the absence of *SsPmp* from records with otherwise proper observation geometries. Finally, we use 2D synthetic seismograms to show that T_{VDSS} is affected not only by crustal thickness at the reflection point, but also by heterogeneity in V_s structure beneath the virtual source and receiver, for instance lateral variation in lithospheric thickness, which must be accounted for when using T_{VDSS} to estimate crustal thickness. Our analyses qualitatively explain the variation of Φ_{VDSS} and A_{VDSS} in our example from the Ordos Plateau. In our companion paper (Liu et al., unpublished manuscript, hereafter “Part 2”), we will discuss practical approaches to inferring lithospheric structure from *SsPmp* observations.

2. Data

The Ordos Plateau in northern China (Fig. 4a) is a site of considerable interest, as it is the surviving remnant of the Archean North China Craton (Liu et al., 1992). It is unknown why this region preserved its lithospheric root while the eastern part of the craton underwent significant modification (decratonization) in Mesozoic time (Gao et al., 2008; Griffin et al., 1998; Menzies et al., 1993). To study the lithospheric structure of the Ordos Plateau, a W–E linear seismic array was deployed across the Ordos Plateau at $\sim 37.5^\circ$ N during 2006–2008 by Peking University (Yu

et al., 2012), and recorded abundant intermediate to deep seismicity in the west-Pacific subduction zones at epicentral distances of 30–50°, making the dataset ideal for observing post-critical *SsPmp* (Fig. 4a). Because the western and eastern parts of the array were deployed in two different time periods, we use two nearby events (~400 km separation) in the Banda Sea to make a single record section (Figs. 4b,c). The radial and vertical-component traces are bandpass filtered between 0.04 and 0.5 Hz, separated into P and SV components with a particle-motion analysis algorithm (Yu et al., 2013) and aligned by their direct S (*Ss*) arrival times. The *Ss* arrival times are picked at the zero-crossings of the *Ss* wavelets, which closely resemble a first-order Hermitian wavelet (first derivative of Gaussian wavelet; Figs. 4b-f), because for a first-order Hermitian wavelet the peak of its envelope function is at its zero-crossing and does not change after an arbitrary phase shift. The sensitivity of measured arrival time to the addition of noise could make the use of the zero-crossing less appropriate for real data than for these synthetics. Our synthetic waveforms are normalized to the peak amplitudes of the corresponding direct S arrivals.

We observe significant variation in *SsPmp* amplitude across the array. For instance, the *SsPmp* amplitude of JB09 is only about half of JB13 (Figs. 4d,e), despite a station separation of only ~60 km. Because the traces are normalized by the peak amplitudes of *Ss*, the effects of source radiation pattern are removed (and should be minor anyway since the aperture of the array is small compared to the epicentral distance). The rapid change of *SsPmp* amplitude across the array thus must be due to structure near the stations. Φ_{VDSS} also varies rapidly across the array. At JB13, *SsPmp* has a ~90° phase advance relative to *Ss* (Fig. 4e), as commonly assumed for post-critical *SsPmp* (Tseng et al., 2009). However, only ~120-km distant, at FY03 the *SsPmp* waveform closely resembles *Ss*, indicating a ~0° phase shift (Fig. 4f). Φ_{VDSS} is unrelated to the source and should be primarily controlled by structure close to the stations. *SsPmp* amplitude and Φ_{VDSS} are crucial properties that need to be correctly modeled in order to measure T_{VDSS} . If the signal-to-noise ratio of *SsPmp* is very small, it will be difficult to measure its arrival time. Even when *SsPmp* amplitude is high, as for JB13 and FY03, improperly modeling the phase of *SsPmp* will cause up to ~1s error in T_{VDSS} , which corresponds to ~5 km error in the resulting crustal thickness estimation, a nontrivial error in most applications. The phenomenon of significant spatial variation of *SsPmp* amplitude and Φ_{VDSS} has not been systematically explored by previous studies. Another unexpected feature of the Ordos dataset is that T_{VDSS} varies significantly across

the array (Fig. 4a). Using the arrival time of the strongest peaks on the P component as an approximation of T_{VDSS} (equivalent to assuming a 90° phase shift), we find that T_{VDSS} reaches its maximum of ~ 12 s at $\sim 110.5^\circ$ E, nominally corresponding to a crustal thickness of ~ 60 km, and then decreases rapidly eastward, reaching ~ 6 s at $\sim 113^\circ$ E, which corresponds to a crustal thickness of ~ 30 km (Yu et al., 2012). This change in travel-time is far greater than possible phase delays that are limited to $0-180^\circ$, or ~ 2 s for these ~ 4 s period arrivals. The unexpectedly deep Moho was previously interpreted as preservation of a ~ 20 -km thick, mafic lower-crustal layer beneath the Ordos Plateau, relict from craton formation (Yu et al., 2012). However, it has recently been recognized that lateral variation in V_s structure can affect T_{VDSS} (Yu et al., 2016), and thus it is important to quantify this effect. In the following sections, we use synthetic seismograms to examine possible lithospheric structures that may affect A_{VDSS} , Φ_{VDSS} and T_{VDSS} .

3. Synthetic Tests

3.1. Sensitivity to V_p across the crust-mantle boundary (CMB)

In this section, we first assume that the lithosphere consists of three homogeneous layers separated by abrupt discontinuities: the upper crust, lower crust and upper mantle (Figs. 5a, 6a). The *SsPmp* waveform is affected by V_p of the lower crust and upper mantle, therefore we first vary V_p^{lc} with fixed V_p^{um} (Fig. 5a), and then vary V_p^{um} with V_p^{lc} fixed (Fig. 6a), to test the sensitivity of the *SsPmp* waveform to the two parameters. As V_p varies, we vary V_s to keep Poisson's ratio ν constant at 0.25, and vary density to satisfy the Nafe-Drake relation (Equation 1 in Brocher, 2005). We compute radial and vertical-component waveforms using the reflectivity algorithm in a layered medium (Randall, 1989), in which the incident S wave is set with ray parameter $p = 0.125$ or 0.130 s/km ($1/p = 8.00$ or 7.69 km/s) in order to test the potential effects of p . The radial and vertical-component waveforms are then separated into S and P components. To separately examine reflections at the CMB and intra-crustal interfaces, which usually interfere with each other, we also compute synthetic wavelets for the reflections separately by directly applying the reflection coefficients at the corresponding interfaces to the incident wavelet (Aki and Richards, 1980b)(Fig. 5c-f, Fig. 6c,d). The only difference between the wavelets computed with this approach and the ones given by the reflectivity method is the S-to-P reflection coefficient at the virtual source, which is constant across all models thus does not affect the comparison between the models. The source time function is assumed to be a first-

order Hermitian wavelet (first derivative of a Gaussian wavelet) with a half width of ~ 2 s, which has similar shape and frequency to observed Ss of deep or intermediate-depth earthquakes (Fig. 4). We note that deconvolving the source wavelet (in this case the first-order Hermitian wavelet) from the radial and vertical components can reduce the source time function to simpler forms (e.g. Gaussian wavelets), which may reduce complexities of the waveforms and naturally align the traces (Parker et al., 2016; Yu et al., 2013). However, deconvolution is a nonunique inversion that can introduce artifacts, so here we avoid it in order to more clearly show the underlying physics of $SsPmp$.

Fig. 5b shows synthetic seismograms computed with V_p^{lc} ranging from 7.0–7.6 km/s, V_p^{um} fixed at 8.1 km/s and $p = 0.125$. This range of V_p^{lc} is characteristic of mafic continental lower crust (Christensen and Mooney, 1995). As V_p^{lc} increases, $SsPmp$ arrives earlier (T_{VDSS} decreases) and becomes closer to the reflection phase at the top of the lower crust ($SsPip$ with i standing for intra-crustal interface; Fig. 5b), with little change in its amplitude or Φ_{VDSS} (Fig. 5d). The amplitude of $SsPip$ grows as V_p^{lc} increases (Fig. 5c), interfering with $SsPmp$ and distorting its waveform (Fig. 5b). The different responses of $SsPip$ and $SsPmp$ to velocity changes indicate their different natures. As a pre-critical reflection, the amplitude of $SsPip$ grows as the velocity contrast at the intra-crustal interface increases. In contrast, as a post-critical reflection phase, the amplitude of $SsPmp$ (a proxy for A_{VDSS}) stays constant despite changes of velocity contrast across the Moho, because all incident energy is reflected upwards at the CMB (V_p^{um} exceeds the ray parameter p). To test the effects of ray parameter, we compute the $SsPmp$ and $SsPip$ wavelets for $p = 0.130$ s/km (Fig. 5a). The $SsPmp$ wavelet for $p = 0.130$ s/km shows significantly smaller Φ_{VDSS} for every V_p^{lc} value than for $p = 0.125$ s/km (Fig. 5d,f). In addition, we observe a significant decrease of Φ_{VDSS} with increasing V_p^{lc} for $p = 0.130$ s/km (Fig. 5f). These observations indicate that ray parameter can have profound effects on Φ_{VDSS} and its sensitivity to V_p^{lc} . As expected, $SsPip$ amplitude increases with increasing p due to a wider incident angle at the intra-crustal discontinuity (Fig. 5e).

Fig. 6 shows the sensitivity of $SsPmp$ waveforms to V_p^{um} . We compute synthetic seismograms using models with V_p^{um} ranging from 8.1–8.7 km/s and V_p^{lc} fixed at 7.0 km/s (Fig. 6a). The range of V_p^{um} used here covers much of the observed range for the continental uppermost mantle (Christensen and Mooney, 1995), and also ensures post-critical reflection of

SsPmp at the CMB for our chosen ray parameters ($1/p=7.69$ and 8.00 km/s). When $p = 0.125$ s/km, our synthetic seismograms show strong dependence of Φ_{VDSS} on V_p^{um} (Fig. 6b). When $V_p^{um} = 8.1$ km/s, Φ_{VDSS} is close to 180° (corresponding to the source wavelet multiplied by -1), and the waveform is similar to the pre-critical reflection. As V_p^{um} increases, Φ_{VDSS} first decreases to $\sim 90^\circ$, and then further drops to below 90° (Fig. 6b,c). Another important observation is that despite the significant change in phase, *SsPmp* amplitude stays almost the same as V_p^{um} increases, because all incident energy is post-critically reflected. When p increases to 0.130 s/km, Φ_{VDSS} decreases and becomes less sensitive to changes of V_p^{um} (Fig. 6d). This observation shows the significant effects of ray parameter on Φ_{VDSS} and its sensitivity to V_p^{um} . Because Φ_{VDSS} (the *SsPmp* waveform) is sensitive to V_p^{um} , one must know V_p^{um} in order to correctly measure T_{VDSS} . An example is shown in Fig. 6e, in which we assume the *SsPmp* wavelet to be phase-shifted by 90° from *Ss*, and cross-correlate it with synthetic waveforms in Fig. 6b to find T_{VDSS} . The resulting T_{VDSS} for each model is then converted to estimated crustal thickness (Moho depth) using Eq. 1 with the true average crustal V_p . We observe that a 90° phase shift is only a good approximation when $V_p^{um} = \sim 8.47$ km/s, whereas for $V_p^{um} = 8.1$ km/s the estimated Moho depth is ~ 3 km larger than the true value (Fig. 6e). This example highlights the importance of using the correct V_p^{um} in measuring T_{VDSS} and estimating Moho depth.

To further explore the effects of ray parameter p on Φ_{VDSS} and its sensitivity to V_p^{lc} and V_p^{um} , we calculate Φ_{VDSS} as functions of V_p^{lc} and V_p^{um} for $p = 0.125$ and 0.130 s/km ($1/p = 8.00$ km/s and 7.69 km/s) by taking the phases of the complex P-to-P reflection coefficients at the Moho (Aki and Richards, 1980a, 1980b). Our first-order observation is that Φ_{VDSS} decreases for all V_p^{lc} and V_p^{um} when p increases from 0.125 to 0.130 s/km (Fig. 7), which agrees with our synthetic waveforms (Fig. 5d,f, Fig 6c,d). In addition, as p increases from 0.125 to 0.130 s/km, Φ_{VDSS} becomes less sensitive to V_p^{um} and more sensitive to V_p^{lc} (contours in Fig. 7 are steeper in (b) than in (a)), which also agrees with our synthetic waveforms (Fig. 5d,f, Fig 6c,d). Moreover, for a fixed p , Φ_{VDSS} decreases with increasing V_p^{um} and V_p^{lc} , and as Φ_{VDSS} decreases it becomes less sensitive to V_p^{um} and more sensitive to V_p^{lc} (contours steepen from lower left to upper right in both Fig. 7a and b). Because $V_p^{lc} < 1/p < V_p^{um}$, increasing p while fixing V_p^{um} and V_p^{lc} or increasing V_p^{um} and V_p^{lc} while fixing p are both equivalent to moving $1/p$ closer to V_p^{lc} and

farther from V_p^{um} . Therefore, Figure 7a shows that when $1/p$ is close to V_p^{um} , Φ_{VDSS} is more sensitive to V_p^{um} than V_p^{lc} (~ 10 times more sensitive to V_p^{um} in bottom left of Fig. 7a as indicated by the reference line), which can be understood by considering that as $1/p$ approaches V_p^{um} , the reflection coefficient approaches the pre-critical value of 180° (sign reverse) phase shift regardless of changes in V_p^{lc} . In contrast, Figure 7b shows that when $1/p$ is close to V_p^{lc} , Φ_{VDSS} is more sensitive to V_p^{lc} than V_p^{um} (~ 5 times more sensitive to V_p^{lc} in top right of Fig. 7b as indicated by the reference line), which can be understood by considering that as $1/p$ approaches V_p^{lc} , V_p^{lc} controls where post-critical reflection occurs between the top of the lower crust and the CMB, and V_p^{um} has no effect. Cases with $1/p$ intermediate between V_p^{lc} and V_p^{um} lie between the two extremes.

3.2. Sensitivity to CMB Thickness

To understand how CMB thickness affects *SsPmp* waveforms, we model the CMB as a transition from $V_p = 6.5$ km/s, typical of crustal rocks, to $V_p = 8.1$ km/s, typical of uppermost-mantle rocks. As before, V_s and density are varied simultaneously with V_p to keep Poisson's ratio at 0.25 and to satisfy the Nafe-Drake relation. The ray parameter p is set as 0.127 s/km ($1/p = 7.87$ km/s), in between the two extreme cases discussed above ($p = 0.125$ and 0.130 s/km). We model the transition zone as a stack of 1-km-thick layers and vary the transition thickness from 0 to 20 km below a fixed top at 40 km (Fig. 8a). Similar models have been used (Braile and Chiang, 1986) to study Moho signatures in active source seismic reflection and refraction data, and to show that amplitude-distance characteristics of the *Pn* and *PmP* phases can be used to estimate the thickness of the CMB transition zone. For post-critical *SsPmp*, as the CMB becomes thicker, there is little change in Φ_{VDSS} (Fig. 8b) until the thickness exceeds the dominant wavelength (Fig. 8c). As the CMB thickens, A_{VDSS} stays stable with a slight increase due to decreased pre-critical P-to-S reflection and transmission at the CMB when it becomes a gradient zone (Fig 8c). This behavior is distinct from that of pre-critical reflected and converted phases at the CMB, which become broader and weaker as the CMB thickens. The clear change in Fig. 8b is that T_{VDSS} becomes larger as the post-critical reflection occurs at greater depth, because in each case the incident wave turns within the CMB where $V_p = 1/p$, so the turning depth becomes larger as the CMB thickness increases (Fig. 8a).

Fig. 9 compares the responses of PRF and VDSS to different CMB thicknesses (Figs. 9a,b). The model in Fig. 9b is identical to the model with a 20-km-thick CMB in Fig. 8a, whereas Fig. 9a is the 0-km-thick CMB model in Fig. 8a with the discontinuity shifted from 40 km to 50 km, so that the centers of the CMBs are at the same depth in Fig. 9a and b. When the incident waves are plane P waves with ray parameters in the range 0.04-0.08 s/km, the computed PRFs are strong and narrow for a discontinuous CMB (Fig. 9c), but broad and weak for a transitional CMB (Fig. 9d) (even the strongest Pms on the PRFs shown here is only $\sim 20\%$ the amplitude of the first arrival). As the CMB thickens, high-frequency components of the incident P waves with wavelengths shorter than the scale of the CMB become insensitive to it, eliminating high-frequency components of Pms . The Pms waveforms stay almost unchanged as the ray parameter varies from 0.04-0.08 s/km for both a sharp CMB (Fig. 9c) and a broad CMB (Fig. 9d). Theoretical Pms arrival times (calculated assuming that conversion occurs at the center of the CMB) closely match the centers of observed Pms , and are very similar at the same ray parameter, for both sharp and broad CMBs (Figs. 9c,d). The above behaviors would also be observed for pre-critical Pmp and $SsPmp$ reflections.

In contrast, post-critical $SsPmp$ is a strong phase with similar amplitude to Ss no matter the CMB is a discontinuity or a broad transition zone (Figs. 9f, 8b,c). The reason that post-critical $SsPmp$ remains strong as the CMB thickens is that all frequency components of the down-going P wave are reflected (or turned) at the depth where, for that ray parameter, V_p reaches the turning velocity. As a result, T_{VDSS} predicted using the reflection depth as the depth where the turning velocity is reached follows the move-out of $SsPmp$ closely in the transitional model (Fig. 9f) and differs significantly from T_{VDSS} in the sharp CMB case (Fig. 9e).

When an incident plane wave turns in a medium with positive vertical velocity gradient, the turning wave will have a 90° phase shift relative to the incident wavelet (Shearer, 1999). However, our synthetic waveforms show that, for CMB thickness < 20 km, Φ_{VDSS} of the transitional models are similar to the discontinuity model with the same p (Figs. 8b, 9e,f), instead of 90° . The reason is that the dominant wavelength of down-going P wave in the CMB (~ 25 km for a dominant frequency of ~ 0.25 Hz) is similar to the CMB thickness (< 20 km), causing Φ_{VDSS} to be insensitive to the presence of the transition zone. Since the transitional models have the same total velocity increase across the CMB as the discontinuity model, Φ_{VDSS} of the transitional models are similar to the discontinuity model at a given p . To further test our hypothesis, we

computed Φ_{VDSS} for CMB thicknesses up to 60 km with the total velocity increase across the CMB the same as the discontinuity model (Fig. 8c). The results show that as CMB thickness exceeds ~ 20 km, Φ_{VDSS} starts to deviate significantly from the discontinuity model ($\Phi_{VDSS} = 119^\circ$), and gradually approaches 90° as CMB thickness further increases (Fig. 8c). This supports our hypothesis that Φ_{VDSS} is similar in both transitional and discontinuity models due to finite-frequency effects. In principal, higher-frequency incident waves would show a more pronounced difference between Φ_{VDSS} produced by a sharp and a broad CMB, though recorded teleseismic S waves seldom have useful energy above 1 Hz. Therefore, we conclude that, for CMB thickness smaller than ~ 25 km, no significant difference exists between Φ_{VDSS} caused by a sharp CMB and by a broad CMB, though the two models cause distinct move-out of T_{VDSS} with p (Fig. 9f).

3.3. Sensitivity to Sedimentary Basins

In the presence of sedimentary basins, we expect the waveforms of $SsPmp$ to be affected by the thickness, velocity, Poisson's ratio ν (or V_p/V_s ratio), and velocity gradient of the sedimentary layer. We next test the sensitivity of $SsPmp$ waveforms to sedimentary basins by varying each of these four parameters, one at a time (Figs. 10a-d). Our reference basin model is a homogeneous layer with $V_p = 4.5$ km/s, $\nu = 0.25$, and thickness = 6 km. For simplicity, we assume the basin has uniform properties both at the virtual source and at the receiver (Fig. 10j). The radial and vertical-component waveforms are separated into P and S components as in previous sections.

3.3.1. Sedimentary-layer thickness

To test the effects of sedimentary-layer thickness on $SsPmp$ waveforms, we vary thickness from 0 km (basement at surface), 3 km (shallow-basin) to 6 km (deep-basin) (Fig. 10a). Both basin cases have similar $SsPmp$ amplitude, clearly lower than the basement case (Fig. 10e). $SsPmp$ arrives increasingly later (T_{VDSS} increases) as the basin becomes deeper, because the basin has lower velocities than the basement (Fig. 10e). Also visible in the two basin cases are the seismic arrivals Sbp (S-to-P conversion phase at the basin-basement interface b) and $SsPbp$ (pre-critical P reflection phase at the basin-basement interface after S-to-P reflection at the free surface) (Fig. 10e), both delayed slightly from Ss . (Note that $PpPbp$ has been used for attempted direct basin imaging, e.g. Yang et al., 2012.) As the basin becomes thicker, Sbp and $SsPbp$ are increasingly delayed from Ss (Fig. 10e). $SsbPmp$ (S-to-P reflection at the basin-basement

interface followed by post-critical reflection at the Moho) is not observed because the velocity contrast at the basin-basement interface is not large enough to generate strong S-to-P reflections (Fig. 10e).

The reduced *SsPmp* amplitude in the presence of sedimentary cover has profound significance, as none of the parameters previously examined (V_p^{lc} , V_p^{um} and CMB thickness) have significant effects on *SsPmp* amplitude, thus cannot explain observations of highly variable *SsPmp* amplitude (Figs. 4d,e). We interpret the low *SsPmp* amplitude in the presence of a sedimentary basin as caused by the low V_s at the virtual source, which reduces the incident angle of the incoming S wave at the free surface and lowers the reflection coefficient between the incident S wave and reflected P wave. (In the extreme case, a vertically incident S wave produces no reflected P wave.) Because it is the reflected P wave at the free surface that is later reflected at the Moho to form *SsPmp*, the sedimentary layer reduces *SsPmp* amplitude. In other words, the “efficiency” of the virtual source decreases due to the sedimentary basin at the virtual source. Because the dominant wavelength of the incident S wave is ~ 10 km in the sedimentary layer, significantly larger than 3 and 6 km, the increase of basin thickness from 3 to 6 km does not greatly increase the affected spectrum. Therefore, *SsPmp* amplitude does not vary significantly when the basin deepens from 3 to 6 km (Fig. 10e).

3.3.2. Sedimentary-layer velocities

To test the effects of sedimentary-layer velocities on *SsPmp* waveforms, we vary V_p in our homogeneous basin from 4.5 km/s (high- V_p case), 3.5 km/s (intermediate- V_p), to 2.5 km/s (low- V_p case) (Fig. 10b). Because we hold ν constant, V_s of the basin changes accordingly. As sedimentary V_p drops, we observe a dramatic decrease in *SsPmp* amplitude (Fig. 10f). In the high- V_p case *SsPmp* is still the dominant phase, whereas in the intermediate and low- V_p cases A_{VDSS} becomes so low that it is hard to distinguish it from other basin phases (Fig. 10f). Another important observation is that in the low- V_p case a strong P phase arrives at ~ 4.5 s, ~ 5 s earlier than predicted T_{VDSS} (Fig. 10f) and could be easily misinterpreted as *SsPmp* due to its high amplitude (\sim twice the amplitude of *SsPmp*). We interpret this strong P arrival as a superposition of *SsPbp* and *SsbPmp* that arrive at approximately the same time. As the velocity contrast at the basin-basement interface increases, the S-to-P reflection at the interface becomes stronger, further increasing *SsbPmp* amplitude. If we increase the CMB depth to 60 km, the temporal separation between *SsPbp* and *SsbPmp* will increase so that they appear as two distinct arrivals

(Fig. S1), thereby supporting our interpretation that the strong P phase at ~ 4.5 s in the low- V_p case is the superposition of $SsPbp$ and $SsbPmp$. In summary, when basin velocity is relatively low and basin thickness is large enough (so that the dominant frequency component of the incident wave is sensitive to the basin), $SsPbp$ and $SsbPmp$ become the dominant P phases and can be easily misidentified as $SsPmp$, which may cause significant errors in Moho depths inferred from T_{VDSS} .

The above examples show that $SsPmp$ amplitude is strongly controlled by basin velocity (Figs. 10a-f), which we interpret as a result of reduced S-to-P reflection coefficient at the virtual source in the presence of sedimentary basins. To further validate our interpretation, we calculate the peak of P-component envelope functions in a 4-s time window around the theoretical T_{VDSS} as a proxy for A_{VDSS} for models with basin V_s varied from 1.45-3.75 km/s (Fig. 10i; sedimentary-layer thickness and ν remain fixed at 6 km and 0.25). We also calculate the S-to-P reflection coefficient at the free surface for a half-space (i.e. no basin) for the same V_s range and $\nu = 0.25$ (Fig. 10i). A comparison of the two values shows near equivalence for $V_s > 2.25$ km/s, suggesting the S-to-P reflection ratio is a primary control on A_{VDSS} (Fig. 10i). As V_s decreases below 2.25 km/s, A_{VDSS} becomes significantly more variable probably due to interference of $SsPmp$ with sedimentary phases that become stronger as V_s decreases. Other factors causing smaller discrepancies between A_{VDSS} and S-to-P reflection ratio likely include transmission loss at the basin-basement interface and finite-frequency effects. In Fig. 10i we also show the peak of P-component waveforms (as opposed to envelope functions) in the same 4-s time window around the theoretical T_{VDSS} . Comparison of the envelope amplitude (A_{VDSS}) with the waveform amplitude shows similar trends and behavior, but the discrepancy in absolute value demonstrates again the need to use the more robust envelope definition of A_{VDSS} .

3.3.3. Sedimentary-layer V_p/V_s

To test the effects of sedimentary Poisson's ratio on $SsPmp$ waveforms, we vary ν from 0.25, 0.275 to 0.3 (Fig. 9c). Increasing ν corresponds to increasing V_p/V_s ratio as:

$$V_p/V_s = \sqrt{\frac{2(1-\nu)}{1-2\nu}} \quad (2)$$

Because we hold basin V_p constant, increasing ν causes basin V_s , thus S-wave incident angle, to decrease. Therefore, the amplitude of $SsPmp$ decreases with increasing sedimentary Poisson's

ratio (Fig. 10g). Although the range of ν used here is quite large and covers most sedimentary rocks (Brocher, 2005), the effect of basin ν on *SsPmp* amplitude is rather limited (Fig 10g). Because T_{VDSS} is only related to V_p in the crust (Eq. 1), despite changes of *SsPmp* amplitude, *SsPmp* arrives at identical times in all three cases (Fig. 10g).

3.3.4 Sedimentary-layer velocity gradient

To test how vertical velocity gradient in sedimentary basins affects *SsPmp* waveforms, we compare results for a constant-velocity basin (homogeneous case) with results from a basin formed of six 1-km-thick layers with velocity linearly increasing from 2.5 km/s at the surface to 6.5 km/s at the basin-basement interface (gradient case) (Fig. 10d) (cf. Parker et al., 2016). Although both basins have the same average velocity, our synthetics show that *SsPmp* amplitude is further reduced in the gradient case (Fig. 10h), presumably because lower V_s at the free surface decreases the S-to-P reflection coefficient for high frequency components, which are more sensitive to shallow structure, at the virtual source (Fig. 10f). Because sedimentary basins commonly have velocities increasing with depth, this example explains why observed *SsPmp* amplitude can be lower than modeled for homogeneous sedimentary layers with equivalent delay times.

3.4. Sensitivity to Lateral Heterogeneity in the Mantle

Yu et al. (2016) discussed the effects of local-scale lateral heterogeneity in the crust and the uppermost mantle on travel-time differences between the up-going S legs of *SsPmp* and *Ss*, which in turn result in deviations in T_{VDSS} from the 1D assumption (Eq. 1). A simple example would be the juxtaposition of thick Archean lithosphere (>200 km) and Phanerozoic lithosphere of normal thickness (~80 km), putatively the case at the boundaries of the Ordos Block (Fig. 4) (Yu et al., 2012). We would like to quantify the effects of such lateral heterogeneity on *SsPmp* waveforms.

We create a 2D model with a constant crustal thickness of 40 km, in order to explore only the effect of mantle heterogeneity on *SsPmp* waveforms (Fig. 11a). The lithosphere comprising both the crust and lithospheric mantle is 80-km thick at each end, and 200-km thick in the center of the model. The 200-km thick lithosphere linearly shallows to 80 km across 200 km, forming two straight ramps dipping at 31° (Fig. 11a). The velocity of the lithospheric mantle is ~5% faster than the asthenosphere (Fischer et al., 2010). We use the SPEC-FEM2D software package

to compute the surface-recorded seismograms of a plane S wave with ray parameter 0.1275 s/km (incident angle of 35° in the asthenosphere) incident on the bottom-left of the model (Komatitsch et al., 2001; Komatitsch and Vilotte, 1998; Tromp et al., 2008). Despite a constant crustal thickness in our model, the synthetic seismograms show significant variation of T_{VDSS} across the recording array (Fig. 11b). On the far left of the array, where both virtual sources and receivers are located above thin lithosphere, $SsPmp$ arrives at ~ 6.9 s (Fig. 11b), in agreement with the 1D prediction. When the receiver is located at the edge of the area with thick lithosphere (blue triangle in Fig. 11a), with the corresponding virtual source (blue star in Fig. 11a) above thinner lithosphere, T_{VDSS} increases to ~ 8 s, significantly later than the 1D model prediction (blue traces in Figs. 11b,c). In the center of the area with thick lithosphere, where receivers and corresponding virtual sources are both in areas with thick lithosphere, observed T_{VDSS} returns to the time predicted for the 1D model (black virtual source, receiver, traces in Figs. 11a-c). At the right edge of the area with thick lithosphere, where the receivers are located above thinner lithosphere than their virtual sources, T_{VDSS} rapidly decreases to ~ 5.5 s, significantly earlier than the 1D prediction (red triangle, star and traces in Figs. 11a-c). If this observed T_{VDSS} is used to infer crustal thickness with an 1D assumption, the 1.5 s difference from the theoretical T_{VDSS} will cause ~ 8 km error in Moho depth. The explanation for the anomalous T_{VDSS} is that when the up-going S wave leg of Ss travels through a velocity anomaly that is not present on the path of $SsPmp$ (Fig. 11d), the travel-time difference between the two ray paths deviate from predictions made by assuming 1D earth structure, and the residual will be included in the observed T_{VDSS} . Therefore, when applying VDSS to data collected in areas with significant variation in lithosphere thickness, it is vital to correct for S travel-time residuals before converting observed T_{VDSS} to crustal thickness. A practical approach to this correction is presented in Part 2.

Another interesting feature of our synthetic seismograms is that the Ss observed above the right margin of the thick lithosphere is significantly stronger than that observed along the rest of the profile (red traces in Figs. 11b,c). The increase in Ss amplitude cannot be due to crustal structure as the crustal thickness is uniform along the profile. Instead, the lithosphere ramp on the right edge of the thick lithosphere causes energy to be focused (multi-pathing effect; see Part 2). Note that we apply no normalization to the traces in Figs. 10b,c. If the traces are normalized with the peak Ss amplitude of each trace, a common practice in VDSS data processing, the red trace at the right edge of thick lithosphere will have a low $SsPmp$ amplitude of 0.83 due to its

high Ss amplitude. In contrast, the blue trace at the left edge of thick lithosphere (Fig 11a-c) will have a high $SsPmp$ amplitude of 1.23. Thus, lateral heterogeneity in the mantle can affect A_{VDSS} , as well as T_{VDSS} , by changing the energy distribution across the incident S wave front.

4. Discussion

The nature of $SsPmp$ as a post-critical, wide-angle reflection phase brings both advantages and disadvantages in using T_{VDSS} to infer Moho depth. A clear advantage of $SsPmp$ compared with narrow-angle phases (e.g. Pms used in PRF) is its high amplitude, which makes it possible to constrain crustal thickness with a single record. In addition, the long ray path of $SsPmp$ in the crust causes T_{VDSS} to have a stronger dependence on ray parameter (or higher “move-out”) than Pms , making it feasible to use the move-out of $SsPmp$ to simultaneously constrain crustal thickness and crustal average V_p (Kang et al., 2016; Parker et al., 2016). In addition, given a uniform azimuthal distribution of earthquakes, it is possible to measure crustal thickness on a circle with ~ 60 -km radius centered at the receiver, a much broader range than the CMB depth sampled by PRFs that is usually within 15 km from the receiver. Moreover, post-critical reflection causes a phase shift Φ_{VDSS} between $SsPmp$ and Ss , which can potentially be used to determine V_p^{lc} and V_p^{um} , though this inference requires particularly high-quality waveform data (see Part 2).

Disadvantages of the long crustal ray path of $SsPmp$ include the sensitivity of $SsPmp$ to lateral variation over a wide area, both in basins near the surface and at mantle depths. For instance, Fig. 10 shows that sedimentary basins at virtual sources can significantly reduce $SsPmp$ amplitude, making it difficult to measure T_{VDSS} . Sedimentary basins may also generate phases ($SsPbp$, $SsbPmp$, etc.) that are stronger than $SsPmp$ and can easily be misidentified as $SsPmp$, thus causing large errors in inferred Moho depths (Fig. 10) (though also offering the ability to study basin structure). Dense 1D or 2D arrays that cover both basins and adjacent exposed basement are key to avoiding such mistakes, because the gradual transition in waveforms allows recognition of sedimentary effects. In a second example, Fig. 11 shows the effect of heterogeneous mantle velocity structure on $SsPmp$ amplitude and T_{VDSS} , which can be partially overcome by application of “static” corrections given data collected by a dense 2D array (Yu et al., 2016). In general, future work using $SsPmp$ to study crustal properties should leverage the power of dense arrays to alleviate challenges posed by its long ray path in the crust.

When the CMB is a transition zone, $SsPmp$ is a turning wave with post-critical reflection at the depth where V_p reaches the turning velocity ($1/p$). Because $SsPmp$ is high amplitude even for a transitional CMB, it is possible to use $SsPmp$ with different ray parameters, which turn at different depths, to constrain the interior structure of the CMB (Fig. 9). In contrast, conversion phases such as Pms (and pre-critical reflection phases) may be too weak to image a transitional CMB. In areas with poorly-defined or absent PRF Moho, such as the Colorado Plateau, analysis of post-critical $SsPmp$ may reveal more details of the CMB.

The Ordos Plateau is overlain by thick west-dipping Phanerozoic strata, with the age of exposed rocks decreasing westward (Xia et al., 2017; Yang et al., 2005). The virtual source of JB09 is west of the virtual source of JB13 (Fig. 4c), so is above younger, thus likely lower-velocity sedimentary rocks. A wide age range of sedimentary rocks may also cause significant velocity gradients across the basin. These factors likely explain the significantly reduced $SsPmp$ amplitude at JB09 compared to JB13. In contrast to the change in $SsPmp$ amplitude between JB09 and JB13, the change in Φ_{VDSS} between JB13 and FY03 may have a more complicated origin. As shown in Figs. 5 and 6, elevated V_p^{lc} and V_p^{um} reduce Φ_{VDSS} and may cause $\Phi_{VDSS} \approx 0^\circ$ at FY03. In addition, if the CMB is dipping from the virtual source towards the station, the incident angle of $SsPmp$ at the Moho is increased, thus increasing ray parameter p and decreasing Φ_{VDSS} (Fig. 7). Because the virtual source of FY03 is closer than station JB13 to the actively extending Shanxi Graben System (Fig 4a), the crust at the virtual source is likely thinner than at the station, causing a dipping CMB that may also contribute to the very small Φ_{VDSS} at FY03. Quantitative analysis of change in $SsPmp$ amplitude and Φ_{VDSS} across the Ordos Plateau is beyond the scope of this paper and will be presented elsewhere.

5. Conclusion

We use synthetic seismograms to show that the phase shift of $SsPmp$ relative to Ss (Φ_{VDSS}) decreases as lower-crust P-wave velocity (V_p^{lc}), upper mantle P-wave velocity (V_p^{um}), or ray parameter increase, making it possible to constrain V_p^{lc} and V_p^{um} with observed $SsPmp$ waveforms. Amplitude of $SsPmp$ (as a proxy for A_{VDSS}) is insensitive to CMB thickness but is strongly affected by near-surface velocity at the virtual source. If the CMB is a velocity gradient zone, $SsPmp$ is a turning wave within the CMB, with turning depth determined by the ray parameter, thereby offering the potential to image the CMB in areas where methods based on

In review with *Geophysical Journal International*

conversion and pre-critical reflection phases fail to show a clear Moho. We also show that T_{VDSS} is affected not only by crustal thickness, but also by crustal and upper-mantle heterogeneity, which requires array data for proper analysis.

Acknowledgements:

Tianze Liu is supported by a Stanford Graduate Fellowship. We thank all the people who were involved in the deployment of the Peking University temporary array in the Ordos Plateau.

References:

- Aki, K., Richards, P.G., 1980a. Phase shifts: phase delay and phase advance, in: *Quantitative Seismology, Theory and Methods, Volume One*. W. H. Freeman and Company, San Francisco, p. 156.
- Aki, K., Richards, P.G., 1980b. Reflection and transmission of P-SV across a solid-solid interface, in: *Quantitative Seismology, Theory and Methods, Volume One*. W. H. Freeman and Company, San Francisco, pp. 144–151.
- Bao, Y., Niu, F., 2017. Constraining sedimentary structure using frequency dependent P-wave particle motion: a case study of the Songliao Basin in NE China. *J. Geophys. Res. Solid Earth*. doi:10.1002/2017JB014721
- Braile, L.W., Chiang, C.S., 1986. The continental Mohorovicic Discontinuity: Results from near-vertical and wide-angle seismic reflection studies, in: *Reflection Seismology: A Global Perspective*. pp. 257–272.
- Brocher, T.M., 2005. Empirical relations between elastic wavespeeds and density in the Earth's crust. *Bull. Seismol. Soc. Am.* 95, 2081–2092. doi:10.1785/0120050077
- Christensen, N.I., Mooney, W.D., 1995. Seismic velocity structure and composition of the continental crust: A global view. *J. Geophys. Res. Solid Earth* 100, 9761–9788. doi:10.1029/95JB00259
- Ferragut, G., Liu, T. and Klemperer, S.L., 2017. Significant Variation of Post-critical SsPmp Amplitude as a Result of Variation in Near-surface Velocity: Observations from the Yellowknife Array. In *AGU Fall Meeting Abstracts*, S31B-0808.
- Fischer, K.M., Ford, H.A., Abt, D.L., Rychert, C.A., 2010. The Lithosphere-Asthenosphere Boundary. *Annu. Rev. Earth Planet. Sci.* 38, 551–575. doi:10.1146/annurev-earth-040809-152438
- Gao, S., Rudnick, R.L., Xu, W.L., Yuan, H.L., Liu, Y.S., Walker, R.J., Puchtel, I.S., Liu, X., Huang, H., Wang, X.R., Yang, J., 2008. Recycling deep cratonic lithosphere and generation of intraplate magmatism in the North China Craton. *Earth Planet. Sci. Lett.* 270, 41–53. doi:10.1016/j.epsl.2008.03.008
- Griffin, W.L., Andi, Z., O'Reilly, S.Y., Ryan, C.G., 1998. Mantle Dynamics and Plate Interactions in East Asia, in: Flower, M.F.J., Chung, S., Lo, C., Lee, T. (Eds.), *Geodynamics Series*. American Geophysical Union, Washington, D. C., pp. 107–126. doi:10.1029/GD027
- Guan, Z., Niu, F., 2017. An investigation on slowness-weighted CCP stacking and its application

- to receiver function imaging. *Geophys. Res. Lett.* 44, 6030–6038.
doi:10.1002/2017GL073755
- Hauser, E.C., Lundy, J., 1989. COCORP deep reflections: Moho at 50 km (16 S) beneath the Colorado Plateau. *J. Geophys. Res.* 94, 7071. doi:10.1029/JB094iB06p07071
- Kang, D., Yu, C., Ning, J., Chen, W., 2016. Simultaneous Determination of Crustal Thickness and *P* Wavespeed by Virtual Deep Seismic Sounding (VDSS). *Seismol. Res. Lett.* 87, 1104–1111. doi:10.1785/0220160056
- Kennett, 1991. B. L. N. and E. R. Engdahl, Traveltimes for global earthquake location and phase identification. *Geophys. J. Int.* 105, 429–465. doi:DOI 10.1111/j.1365-246X.1991.tb06724.x
- Kind, R., Kosarev, G.L., Petersen, N. V, 1995. Receiver functions at the stations of the German Regional Seismic Network (GRSN). *Geophys. J. Int.* 121, 191–202. doi:10.1111/j.1365-246X.1995.tb03520.x
- Komatitsch, D., Martin, R., Tromp, J., Taylor, M.A., Wingate, B.A., 2001. Wave propagation in 2-D elastic media using a spectral element method with triangles and quadrangles. *J. Comput. Acoust.* 9, 703–718. doi:10.1142/S0218396X01000796
- Komatitsch, D., Vilotte, J.-P., 1998. The Spectral Element Method : An Efficient Tool to Simulate the Seismic Response of 2D and 3D Geological Structures. *Bull. Seismol. Soc. Am.* 88, 368–392.
- Langston, C. a., 1979. Structure under Mount Rainier, Washington, inferred from teleseismic body waves. *J. Geophys. Res.* 84, 4749. doi:10.1029/JB084iB09p04749
- Langston, C.A., 2011. Wave-field continuation and decomposition for passive seismic imaging under deep unconsolidated sediments. *Bull. Seismol. Soc. Am.* 101, 2176–2190. doi:10.1785/0120100299
- Liu, D.Y., Nutman, A.P., Compston, W., Wu, J.S., Shen, Q.H., 1992. Remnants of Greater-Than-or-Equal-to 3800 Ma Crust in the Chinese Part of the Sino-Korean Craton. *Geology* 20, 339–342. doi:10.1130/0091-7613(1992)020<0339:romcit>2.3.co;2
- Liu, T., Yu, C., Klemperer, S.L., Ning, J., 2015. Lateral Variation of Crustal Structure Beneath a Stable Craton: Seismic Evidence from Ordos, China. In *AGU Fall Meeting Abstracts*, T11B-2893.
- Menzies, M. a., Fan, W., Zhang, M., 1993. Palaeozoic and Cenozoic lithoprobes and the loss of >120 km of Archaean lithosphere, Sino-Korean craton, China. *Geol. Soc. London, Spec. Publ.* 76, 71–81. doi:10.1144/GSL.SP.1993.076.01.04
- Owens, T.J., Taylor, S.R., 1984. A Detailed Analysis of Broadband P Waveforms 89, 7783–7795.
- Parker, E.H., Hawman, R.B., Fischer, K.M., Wagner, L.S., 2016. Estimating crustal thickness using SsPmp in regions covered by low-velocity sediments: Imaging the Moho beneath the Southeastern Suture of the Appalachian Margin Experiment (SESAME) array, SE Atlantic Coastal Plain. *Geophys. Res. Lett.* 43, 9627–9635. doi:10.1002/2016GL070103
- Randall, G.E., 1989. Efficient calculation of differential seismograms for lithospheric receiver functions. *Geophys. J. Int.* 99, 469–481. doi:10.1111/j.1365-246X.1989.tb02033.x
- Shearer, P.M., 1999. Turning Points and Hilbert Transforms, in: *Introduction to Seismology*. Cambridge University Press, pp. 106–109.
- Shen, W., Ritzwoller, M.H., Schulte-Pelkum, V., 2013. A 3-D model of the crust and uppermost mantle beneath the Central and Western US by joint inversion of receiver functions and surface wave dispersion. *J. Geophys. Res. Solid Earth* 118, 262–276. doi:10.1029/2012JB009602

- Tao, K., Liu, T., Ning, J., Niu, F., 2014. Estimating sedimentary and crustal structure using wavefield continuation: Theory, techniques and applications. *Geophys. J. Int.* 197, 443–457. doi:10.1093/gji/ggt515
- Tian, X., Chen, Y., Tseng, T.L., Klemperer, S.L., Thybo, H., Liu, Z., Xu, T., Liang, X., Bai, Z., Zhang, X., Si, S., Sun, C., Lan, H., Wang, E., Teng, J., 2015. Weakly coupled lithospheric extension in southern Tibet. *Earth Planet. Sci. Lett.* 430, 171–177. doi:10.1016/j.epsl.2015.08.025
- Tromp, J., Komatitsch, D., Liu, Q., 2008. Spectral-element and adjoint methods in seismology. *Commun. Comput. Phys.* 3, 1–32.
- Tseng, T.L., Chen, W.P., Nowack, R.L., 2009. Northward thinning of Tibetan crust revealed by virtual seismic profiles. *Geophys. Res. Lett.* 36, 1–5. doi:10.1029/2009GL040457
- Xia, B., Thybo, H., Artemieva, I.M., 2017. Seismic crustal structure of the North China Craton and surrounding area: Synthesis and analysis. *J. Geophys. Res. Solid Earth* 5181–5207. doi:10.1002/2016JB013848
- Yang, Y., Li, W., Ma, L., 2005. Tectonic and stratigraphic controls of hydrocarbon systems in the Ordos basin: A multicycle cratonic basin in central China. *Am. Assoc. Pet. Geol. Bull.* 89, 255–269. doi:10.1360/10070404027
- Yang, Z., Sheehan, A.F., Yeck, W.L., Miller, K.C., Erslev, E.A., Worthington, L.L., Harder, S.H., 2012. Imaging basin structure with teleseismic virtual source reflection profiles. *Geophys. Res. Lett.* 39, 2–7. doi:10.1029/2011GL050035
- Yu, C., Chen, W.P., van der Hilst, R.D., 2016. Constraints on residual topography and crustal properties in the western United States from virtual deep seismic sounding. *J. Geophys. Res. Solid Earth* 121, 5917–5930. doi:10.1002/2016JB013046
- Yu, C.Q., Chen, W.P., Ning, J.Y., Tao, K., Tseng, T.L., Fang, X.D., John Chen, Y., van der Hilst, R.D., 2012. Thick crust beneath the Ordos plateau: Implications for instability of the North China craton. *Earth Planet. Sci. Lett.* 357–358, 366–375. doi:10.1016/j.epsl.2012.09.027
- Yu, C.Q., Chen, W.P., Van Der Hilst, R.D., 2013. Removing source-side scattering for virtual deep seismic sounding (VDSS). *Geophys. J. Int.* 195, 1932–1941. doi:10.1093/gji/ggt359
- Yu, Y., Song, J., Liu, K.H., Gao, S.S., 2015. Determining crustal structure beneath seismic stations overlying a low-velocity sedimentary layer using receiver functions. *J. Geophys. Res. B Solid Earth* 3208–3218. doi:10.1002/2014JB011610

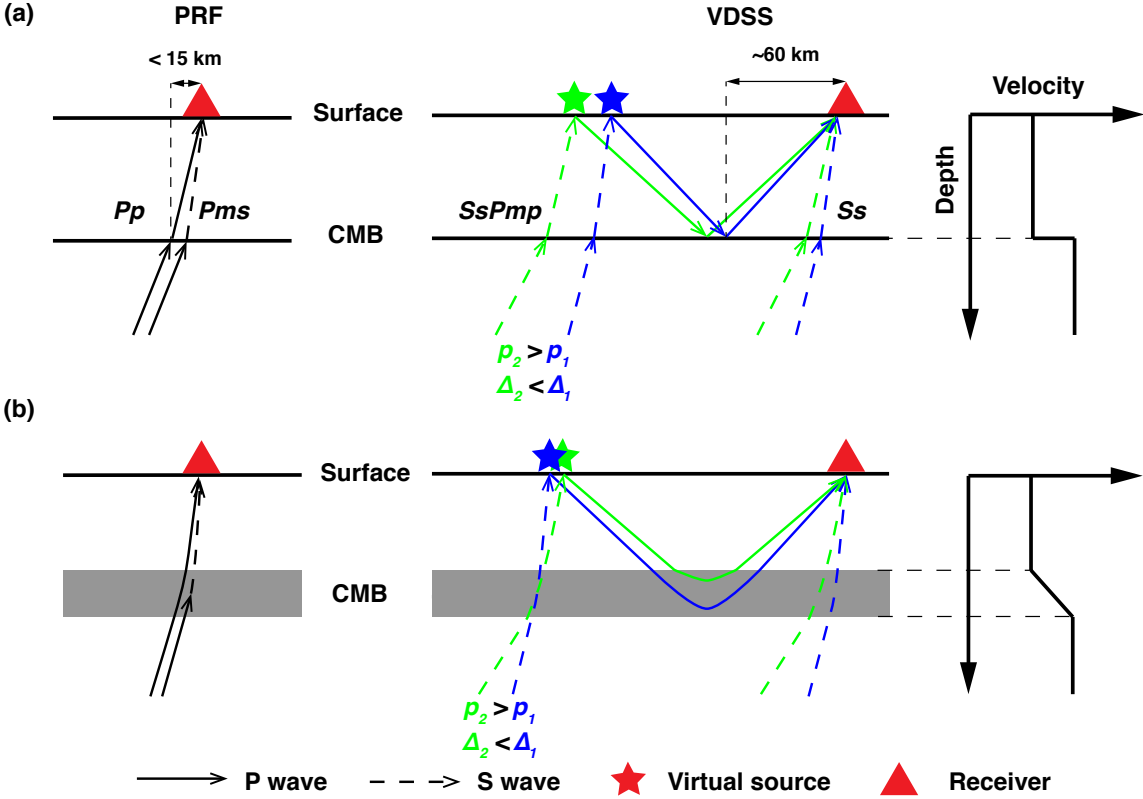


Figure 1. Comparison between ray paths for P receiver functions (PRF; left column) and Virtual Deep Seismic Sounding (VDSS; right column) (a) for an abrupt velocity discontinuity at the crust-mantle boundary (CMB) and (b) for a velocity gradient zone at the CMB. For VDSS, blue and green colors are for earthquakes with epicentral distance Δ_1 and Δ_2 (or ray parameter p_1 and p_2), respectively.

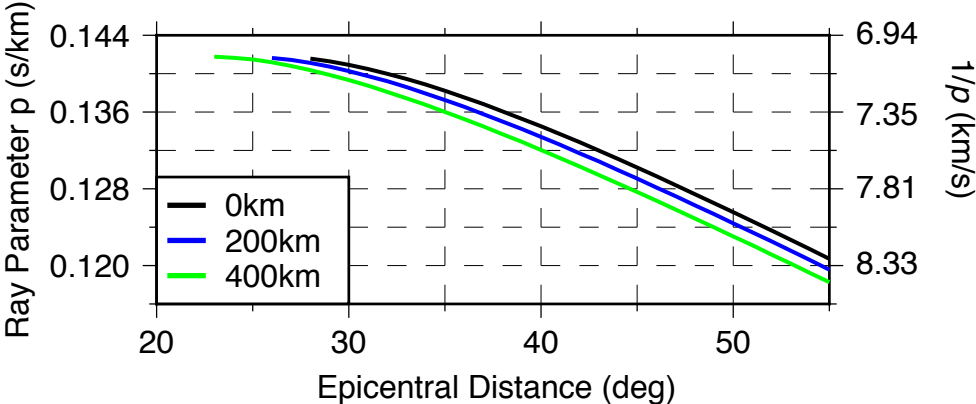


Figure 2. Ray parameter of teleseismic S wave (S_s) as a function of epicentral distance, for focal depths at 0, 200 and 400 km. Ray parameters are calculated using the IASP91 reference model (Kennett and Engdahl, 1991). Note that ray parameters do not exceed 0.143 s/km in order to avoid triplication at the bottom of the mantle transition zone.

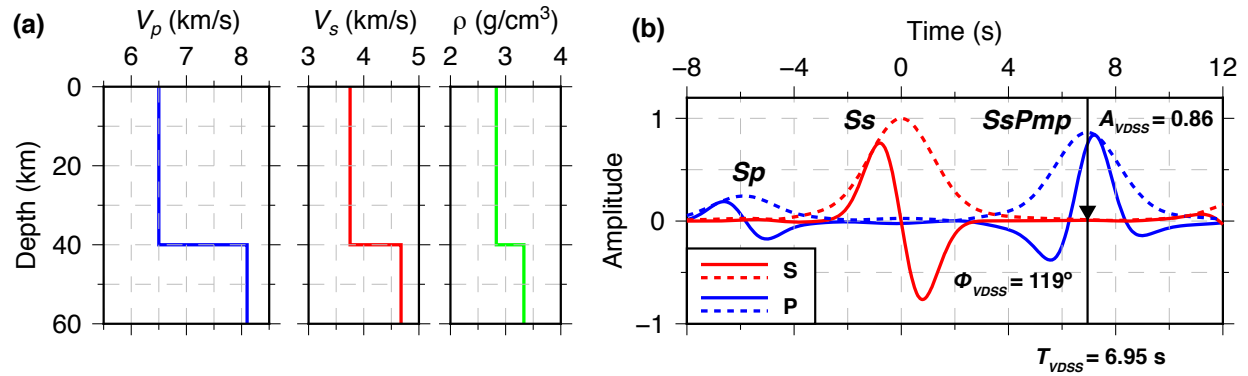


Figure 3. Synthetic post-critical *SsPmp* waveforms (a): 1D velocity and density structure of a homogeneous crust over a half-space mantle used to compute waveforms in (b). (b): P and S-component waveforms (solid) and their envelope functions (dashed) computed using models in (a) and aligned to *Ss* arrival. The ray parameter of the incident S wave is $p = 0.127$ s/km ($1/p=7.87$ km/s). The source time function is a first order Hermitian function with a dominant frequency of ~ 0.25 Hz. The *Ss* arrival is picked at the zero-crossing of the source wavelet or the peak of the envelope function. The waveforms are normalized by the peak amplitude of the *Ss* envelope function, so that A_{VDSS} is clearly shown. Black triangle marks the theoretical *SsPmp* arrival time relative to *Ss* (T_{VDSS}). The large amplitude and phase shift of *SsPmp* is due to post-critical reflection at the Moho.

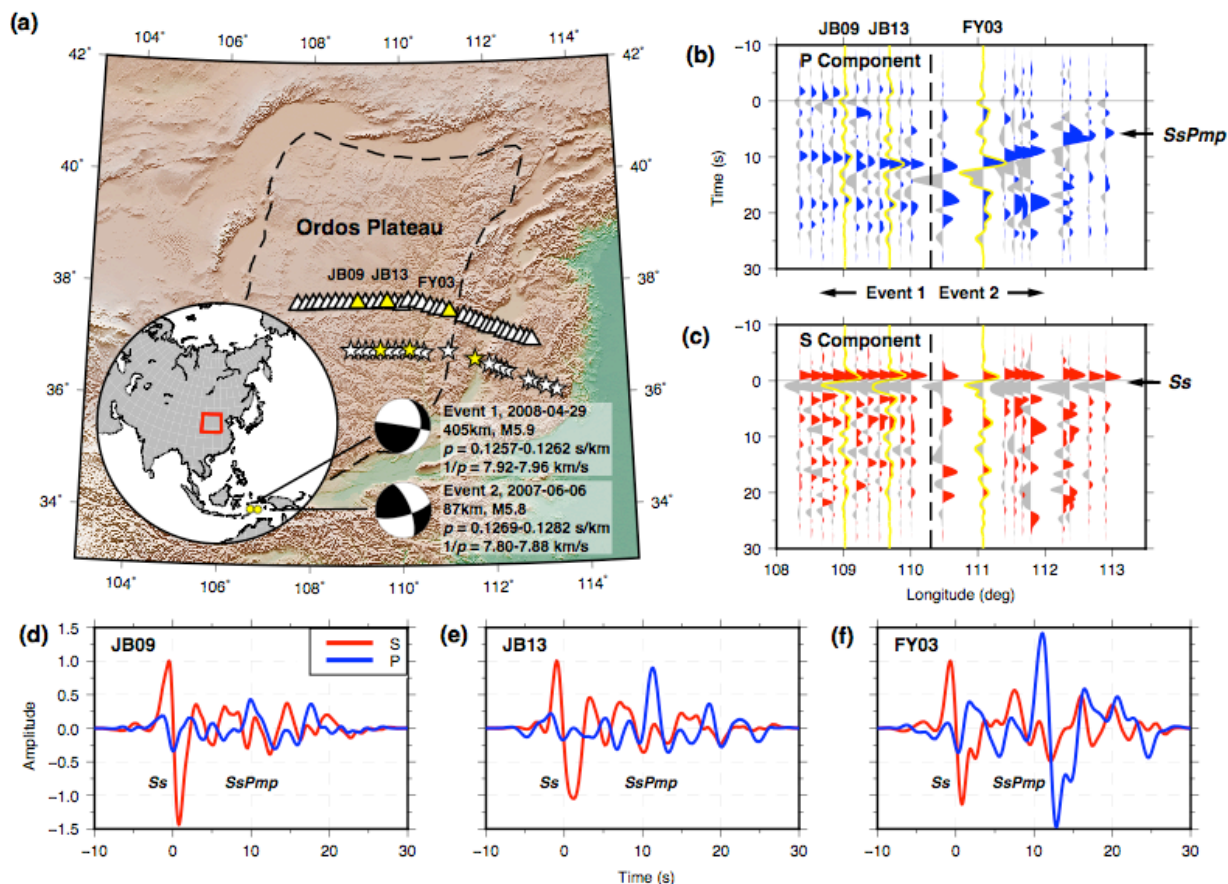


Figure 4. *SsPmp* observations from the Ordos Plateau, North China. (a): broadband seismic stations (triangles) and their corresponding virtual sources (stars) for two closely spaced deep-focus Banda Sea earthquakes, Events 1 and 2. Virtual source locations are calculated using a crustal thickness of 40 km and $V_p = 6.3$ km/s. Yellow triangles and stars correspond to yellow-highlighted traces in (b) and (c) shown enlarged in (d) and (e). Lower-left inset shows location of Events 1 and 2 (yellow circles). The range of ray parameters (ρ) shown is for the entire array. (b): A composite profile of P component of the S wave train from Event 1 (recorded west of 110.3°E) and Event 2 (recorded east of 108.3°E). (c): The same as (b) but for the SV component. P and SV-component waveforms are both aligned by the *Ss* phase (0s, picked at the zero-crossing) and normalized by its maximum amplitude. Dashed vertical lines separate the parts of the array that recorded each of the two events. (d-f): enlargements of yellow-highlighted traces in (b) and (c). Note the significant difference in *SsPmp* amplitude between JB09 and JB13, and the difference in Φ_{VDSS} between JB13 ($\sim 90^\circ$ phase shift from *Ss*) and FY03 ($\sim 0^\circ$ phase shift).

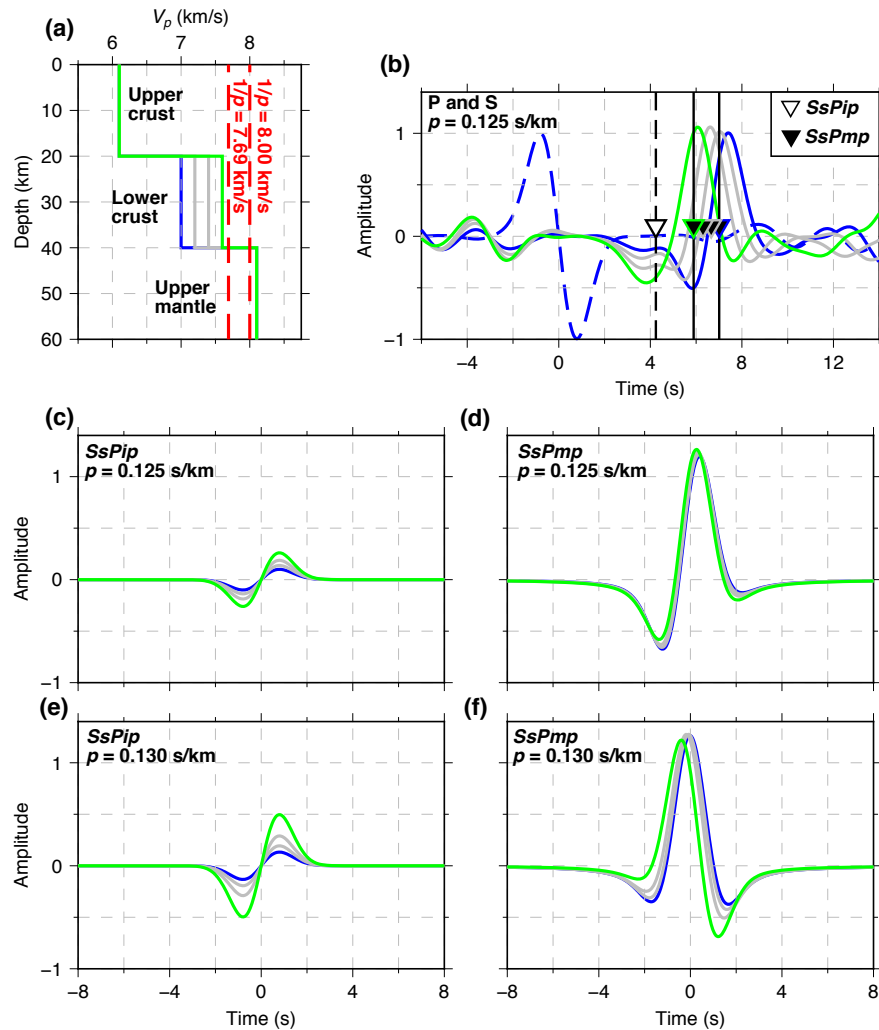


Figure 5. $SsPmp$ waveforms computed for ray parameter $p = 0.125$ and 0.130 s/km and V_p^{lc} ranging from 7.0–7.8 km/s. (a): V_p models used to compute the $SsPmp$ synthetic waveforms. Blue: $V_p^{lc} = 7.0$ km/s. Green: $V_p^{lc} = 7.6$ km/s. Gray: intermediate models. Red dashed lines: critical V_p of the incident waves. (b): Blue, gray and green curves: P-component synthetic waveforms computed with $p = 0.125$ s/km, colored as in (a). Dashed blue curve: S-component synthetic waveform computed with $V_p^{lc} = 7.0$ km/s. Black triangles: theoretical T_{VDSS} for each synthetic waveform. Open triangle: theoretical arrival time of the pre-critical intra-crustal reflection ($SsPip$), constant for all models. (c) and (d): $SsPip$ and $SsPmp$ wavelets respectively computed with $p = 0.125$ s/km, colored as in (b). (e) and (f): the same as (c) and (d) except for ray parameter $p = 0.130$ s/km. Note V_p^{lc} has a stronger effect on Φ_{VDSS} for larger ray parameter.

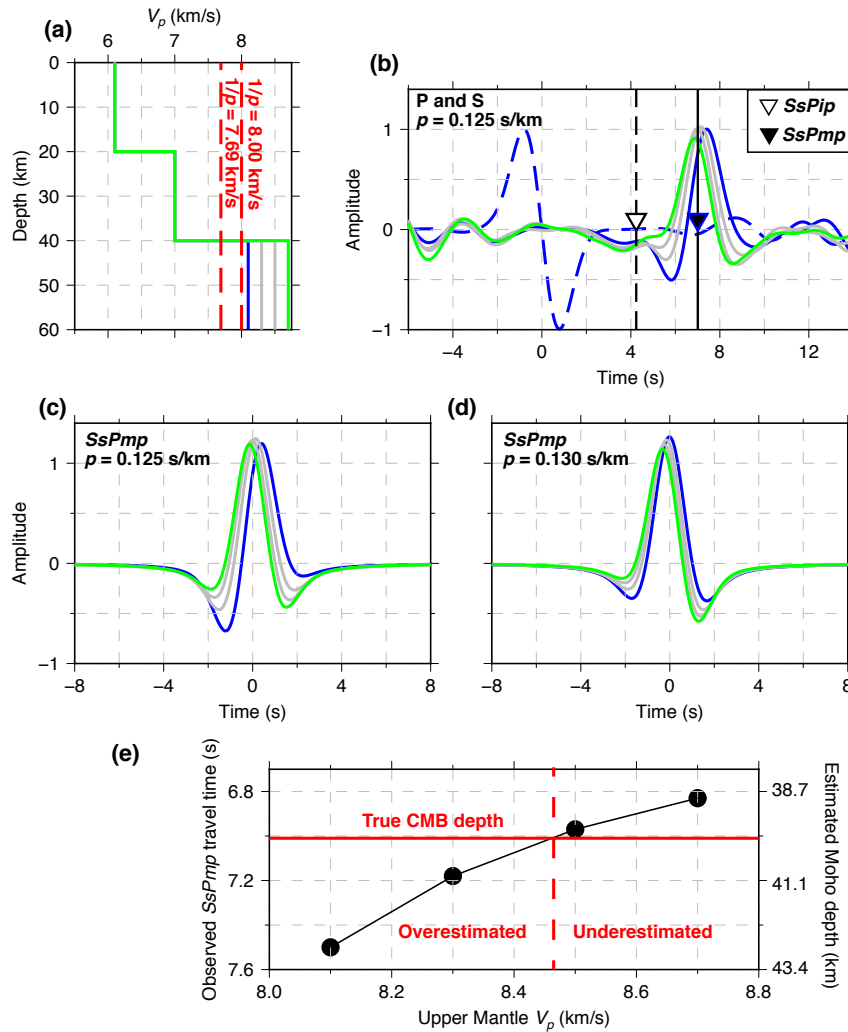


Figure 6. $SsPmp$ waveforms computed for ray parameter $p = 0.125$ and 0.130 s/km and V_p^{um} ranging from 8.1-8.7 km/s. (a): V_p models. Blue: $V_p^{um} = 8.1$ km/s. Green: $V_p^{um} = 8.7$ km/s. Gray: intermediate models. Red dashed line: critical V_p of the incident waves. (b): Blue, gray and green curves: P-component synthetic waveforms colored as in (a). Dashed blue curve: S-component synthetic waveform for $V_p^{um} = 8.1$ km/s. Black (and open) triangles: theoretical T_{VDSS} (and $SsPip$), constant for all models. (c) and (d): $SsPmp$ wavelets computed with $p = 0.125$ s/km and 0.130 s/km, colored as in (b). Note that V_p^{um} has a stronger effect on Φ_{VDSS} for smaller ray parameter. (e): Black dots: observed T_{VDSS} and estimated Moho depth for waveforms in (b) assuming a 90° phase shift of $SsPmp$ relative to Ss. Red line: true CMB depth of 40 km.

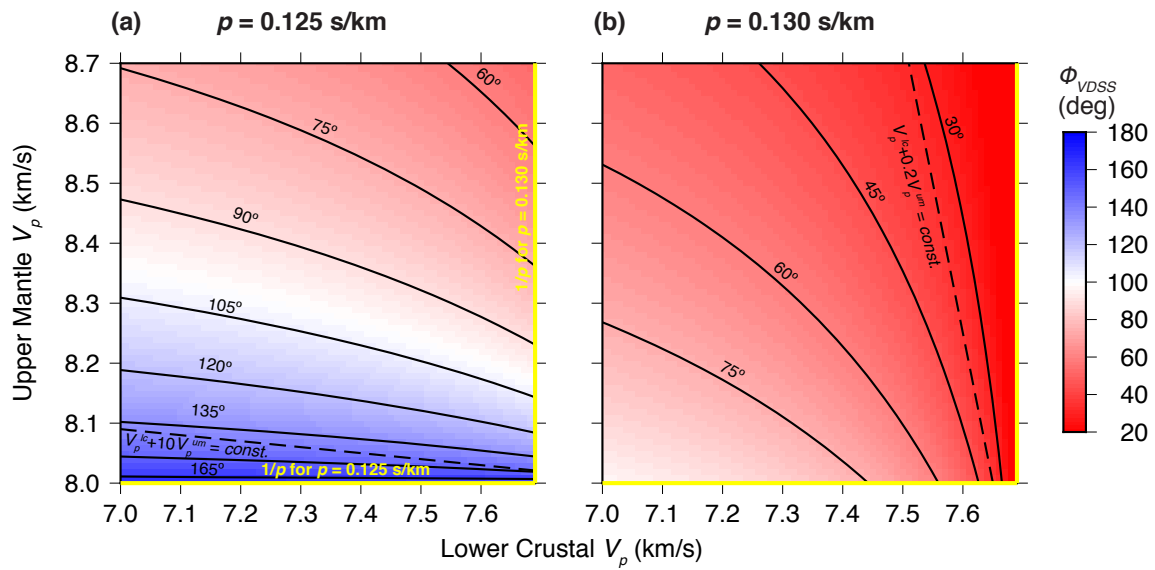


Figure 7. Φ_{VDSS} contoured at 15° intervals, as functions of V_p^{lc} and V_p^{um} for (a) $p = 0.125$ s/km and (b) $p = 0.130$ s/km. V_s and densities are varied to keep a constant Poisson's ratio of 0.25, and to satisfy the Nafe-Drake relation (Brocher, 2005), respectively. Two linear trade-off relations between V_p^{lc} and V_p^{um} are plotted in black dashed lines for reference. Yellow lines: critical velocities for $p = 0.125$ and 0.130 s/km. Note that when $1/p$ is close to V_p^{um} , Φ_{VDSS} is primarily sensitive to V_p^{um} (contours with low slopes, bottom of (a)), whereas when $1/p$ is close to V_p^{lc} , Φ_{VDSS} is primarily sensitive to V_p^{lc} (contours with high slopes, right side of (b)).

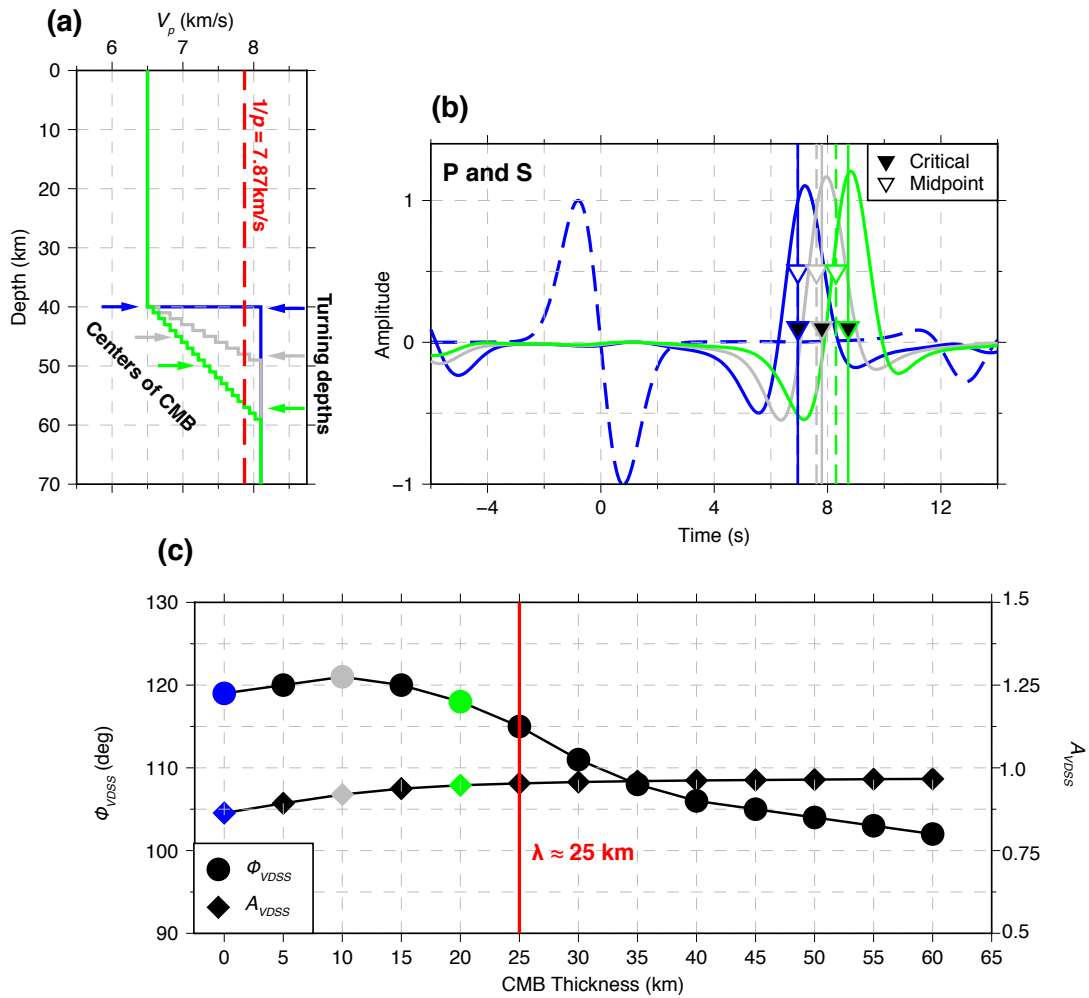


Figure 8. Effects of CMB thickness on *SsPmp* waveforms. (a): V_p models. Blue: CMB as a velocity discontinuity at 40-km depth. Grey: 10-km thick CMB. Green: 20-km thick CMB. V_p at the top and bottom of the CMB are fixed at 6.5 and 8.1 km/s. Red dashed line: critical V_p of the incident wave. (b): Blue, grey and green curves: P-component synthetic waveforms colored as in (a). Dashed blue curve: S-component synthetic seismogram computed with the discontinuous CMB model plotted for reference (*Ss* is essentially identical for all three models). Solid vertical lines and black triangles with blue, grey and green edges: theoretical T_{VDSS} of the models colored as in (a), calculated for the depths at which $V_p = 7.87$ km/s, i.e. at which V_p equals the turning velocity ($1/\rho$). Dashed vertical lines and open triangles with blue, grey and green edges: theoretical T_{VDSS} calculated for the depths to the center of the CMB. (c): Φ_{VDSS} (circles) and A_{VDSS} (diamonds) as functions of CMB thickness. V_p at the top and bottom of the CMB are fixed at 6.5 and 8.1 km/s. Blue, gray and green: models colored as in (a). Red vertical line: dominant wavelength λ of P waves with dominant frequency 0.25 Hz in the CMB. Note that as CMB thickness becomes larger than λ , Φ_{VDSS} deviates significantly from the value with a velocity discontinuity.

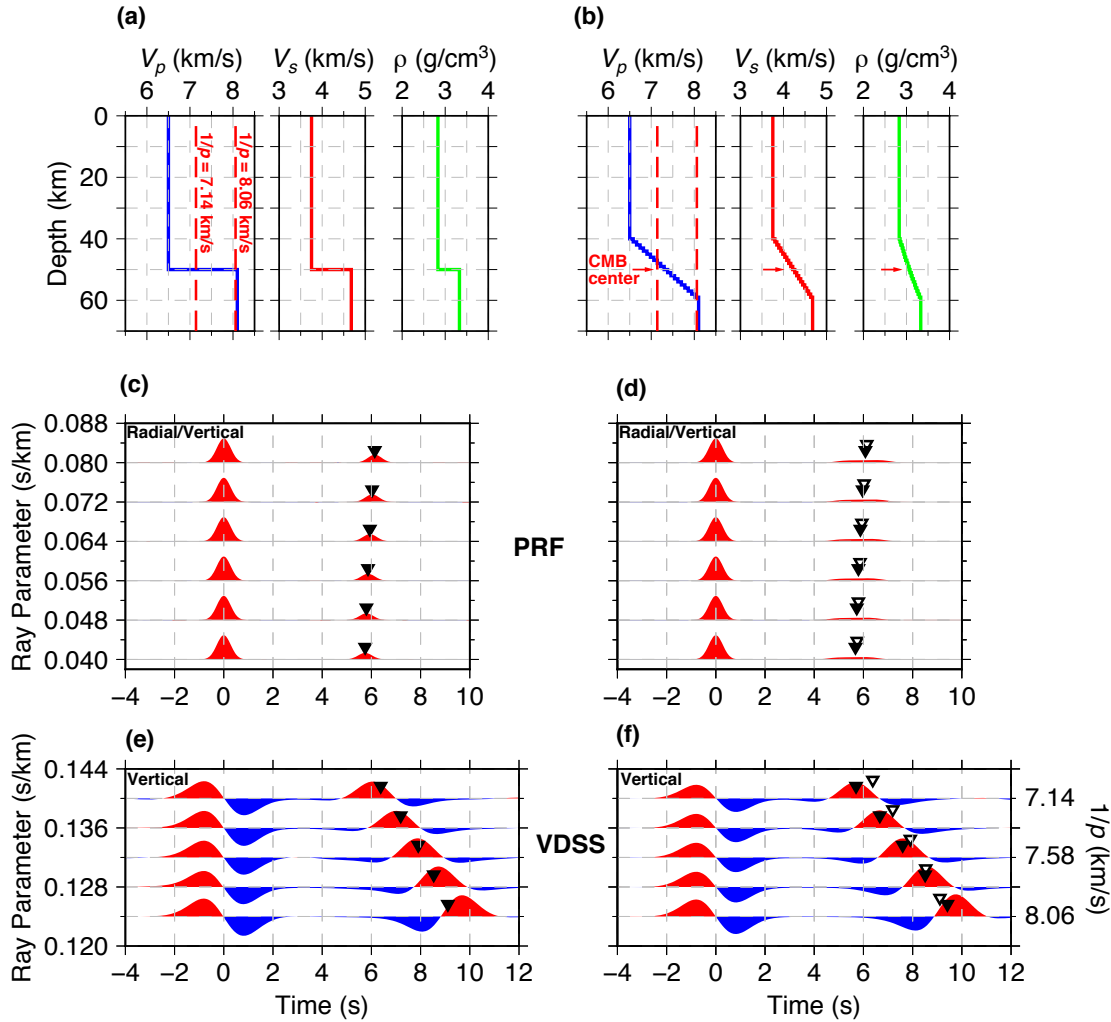


Figure 9. Synthetic RF and $SsPmp$ waveforms with different ray parameters for different CMB thicknesses but the same total velocity change across the CMB. (a) and (b): 1D Models in which the CMB is represented by either a discontinuity in V_p , V_s and density, or by a 20-km thick transition zone. (c) and (d): Synthetic PRFs (radial components deconvolved by vertical components) computed with the models in (a) and (b), and ray parameters ranging from 0.04-0.08 s/km. Black triangles are theoretical Pms travel times for a conversion depth at 50 km, i.e. at the abrupt discontinuity (model a) or at the center of the transition zone (model b). Open triangles in (d) show the theoretical arrival times in model a, offset vertically to be visible. (e) and (f): Vertical-component synthetic $SsPmp$ waveforms computed with models in (a) and (b), and ray parameters ranging from 0.124-0.140 s/km. The corresponding turning velocities ($1/p$) are labeled on the right. Black triangles in (e) are theoretical T_{VDSS} for reflections at the discontinuity, and in (f) are theoretical T_{VDSS} computed for reflections at the depth where $V_p = 1/p$. Open triangles in (f) show T_{VDSS} in (e), offset vertically to be visible. Note that theoretical T_{VDSS} in (e) and (f) form distinct move-out curves with respect to p , and that Φ_{VDSS} varies with p .

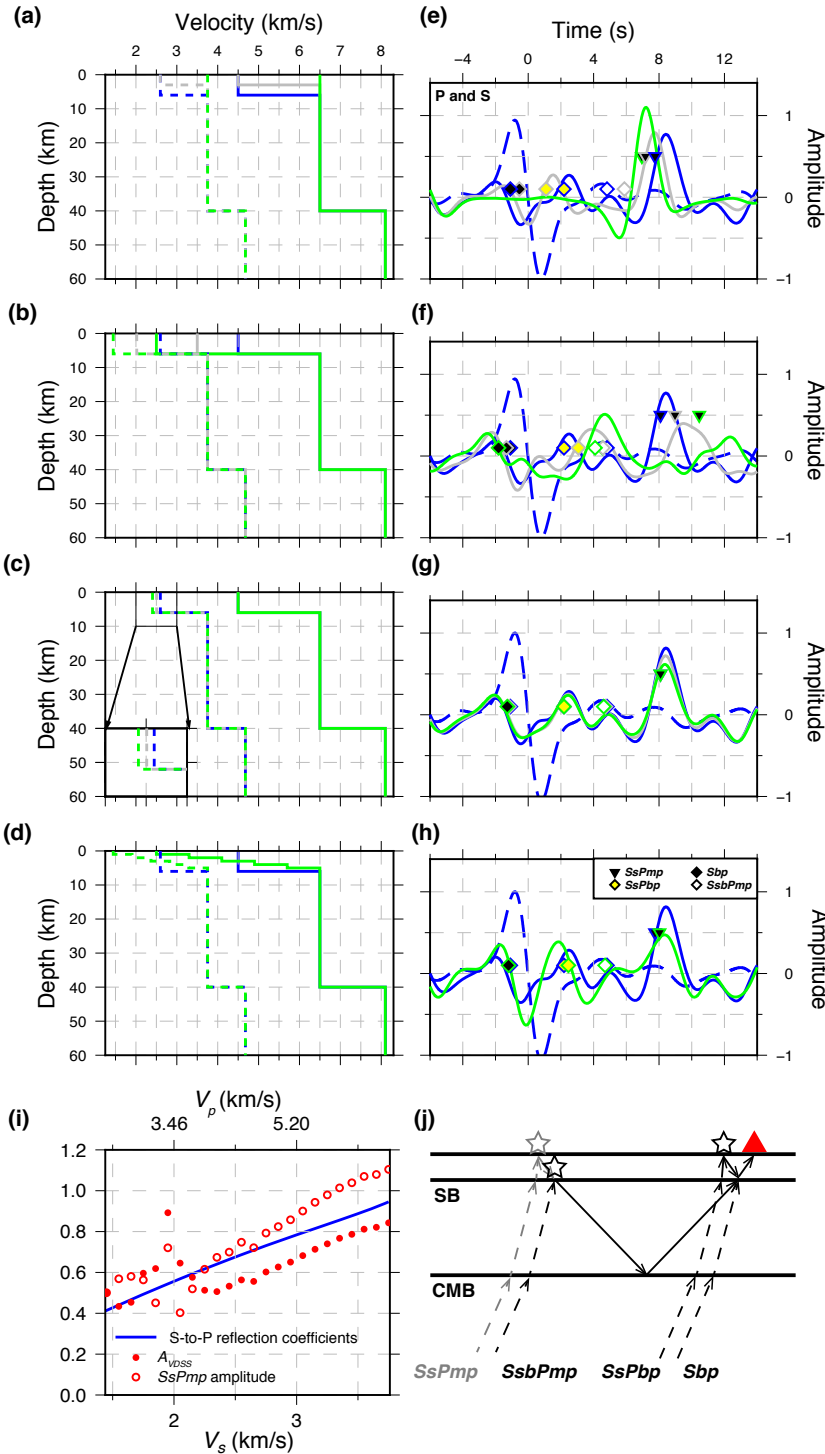


Figure 10. $SsPmp$ waveforms for different sedimentary basins on top of the same crust with 40-km-deep CMB. (a), (b), (c) and (d): V_p (solid lines) and V_s (dashed lines). Blue lines: reference model, 6-km thick basin ($V_p = 4.5$ km/s, Poisson's ratio $\nu = 0.25$) above basement ($V_p = 6.5$ km/s, $\nu = 0.25$) and a CMB discontinuity at 40 km depth above $V_p^{um} = 8.1$ km/s, $\nu = 0.25$. In (a) sedimentary thickness varies: 6 km (blue), 3 km (gray), 0 km (no sedimentary layer, green). In (b) sedimentary V_p varies: 4.5 km/s (blue), 3.5 km/s (gray), 2.5 km/s (green). V_s is varied simultaneously to keep Poisson's ratio at 0.25. In (c) sedimentary Poisson's ratio varies: 0.25 (blue), 0.275 (gray), 0.3 (green), with constant sedimentary $V_p = 4.5$ km/s (see enlarged inset). In (d), the velocity gradient varies: constant velocity (blue), stack of six 1-km thick layers with V_p linearly increasing with depth from 1.5-6.5 km/s (green). (e), (f), (g), and (h): Solid curves: P-component synthetic waveforms for velocity models (a), (b), (c) and (d). Dashed blue curves: S-component synthetic waveforms for the standard model. Black triangles with edges colored corresponding to the velocity models mark theoretical T_{VDSS} . Black, yellow and white diamonds with edges colored corresponding to the velocity models mark theoretical arrival times of Sbp , $SsPbp$, and $SsbPmp$ phases. (i): Effects of sedimentary basin on $SsPmp$ amplitude. Red solid circles: A_{VDSS} for models with sedimentary V_s ranging from 1.45-3.75 km/s (with fixed basin thickness of 6 km and $\nu = 0.25$, i.e. part b). Red empty circles: $SsPmp$ amplitude for the same models. Blue curve: S-to-P reflection coefficient at the free surface for a half-space (i.e. no basin) for the same V_s range and $\nu = 0.25$. Corresponding sedimentary V_p are plotted on the top. (j): Ray paths of $SsPmp$, Sbp , $SsPbp$ and $SsbPmp$.

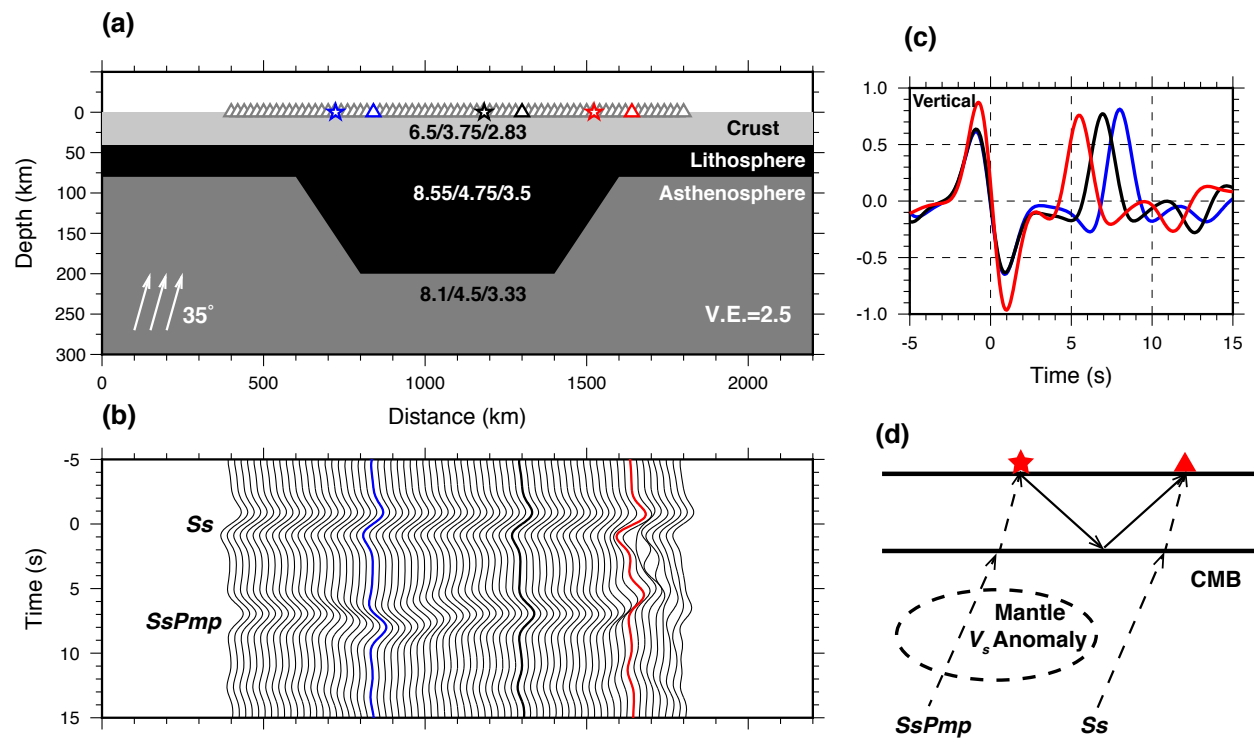


Figure 11. Effects of lateral variation in mantle V_s on T_{VDSS} . (a): 2D model used to compute synthetic seismograms, with a vertical exaggeration of 2.5. Light gray: crust. Black: lithospheric mantle. Dark gray: asthenosphere. Material properties of model layers are listed as V_p (km/s)/ V_s (km/s)/ ρ (g/cm³). Incident angle of the plane S wave is 35°, and the dip of the lithosphere-asthenosphere boundary is 31°. The seismograms of the stations highlighted with blue, black and red are shown in (b) and (c). Stars show the virtual sources of the stations highlighted with the same colors. (b): Vertical-component synthetic seismograms (*not* P- or S-components as shown in all other figures) recorded by stations in (a). Black, blue and red traces: traces recorded by highlighted stations in (a) and colored accordingly. Note the significant lateral variation of T_{VDSS} despite homogeneous crustal thickness. Amplitudes are relative to largest amplitude on plot (*not* normalized by peak Ss amplitude of each trace). (c): Vertical-component synthetic seismograms recorded by highlighted stations in (a) and colored accordingly. (d): Schematic showing V_s anomaly in the mantle affects T_{VDSS} by changing the relative travel times of Ss and the S legs of SsPmp.